X-*CaD*: Explainable AI for Skin Cancer Diagnosis in Healthcare 4.0 Telesurgery

Fenil Ramoliya*, Keyaba Gohil†, Aditya Gohil‡, Riya Kakkar§, Rajesh Gupta¶, *Member, IEEE*, Sudeep Tanwar‖, *Senior Member, IEEE* *†‡§¶‖Department of Computer Science and Engineering, Institute of Technology, Nirma University, Gujarat, 382481, India Emails: *21bce244@nirmauni.ac.in, †21bce076@nirmauni.ac.in, ‡21bce011@nirmauni.ac.in, §21ftphde56@nirmauni.ac.in, ¶rajesh.gupta@nirmauni.ac.in, ‖sudeep.tanwar@nirmauni.ac.in

Abstract—The advent of Healthcare 4.0 has catalyzed a paradigm shift in medical practices, ushering in innovative approaches such as telesurgery, a groundbreaking method for remote patient surgery and monitoring. This transformative technique extends beyond traditional surgeries, finding application in dermatological procedures. The success of telesurgery in skin-related surgeries hinges on accurate and efficient skin cancer detection using dermoscopic images. Recognizing the inherent complexities in interpreting deep learning models, especially in the context of healthcare, Explainable Artificial Intelligence (X-AI) becomes imperative. In this context, we propose a novel CNN-powered X-AI mechanism i.e., X-*CaD*, tailored for skin cancer detection in telesurgery environments, leveraging ResNet and MobileNet for feature extraction. To enhance interpretability and bridge the gap between model predictions and clinical decision-making, we employ X-AI techniques such as Local Interpretable Model-agnostic Explanations (LIME) and Integrated Gradient (IG). LIME provides granular insights into model predictions, elucidating decision-making processes, while IG offers a comprehensive view of feature attributions. X-*CaD* relies on the synergistic integration of advanced CNN architectures with X-AI techniques to identify skin cancer accurately and provide clinicians with clear insights. This represents a significant advancement in the integration of state-of-the-art technology and healthcare, offering a dependable telesurgery solution for the diagnosis of skin cancer in surgical procedures.

Index Terms—Telesurgery, X-AI, Skin cancer, CNN, LIME, IG

I. INTRODUCTION

In recent years, there has been a noticeable trend towards the integration of technology with the healthcare sector. The emergence of smart healthcare has provided medical professionals with the tools and technology to make more concrete diagnoses as well as provided a faster, dependable, and efficient way to conduct various medical procedures. The stages in this advancement [1] can be listed from when they began with Healthcare 1.0 which involved clinical professionals manually recording patient data. This was followed by Healthcare 2.0 where the storage of health records was made digital. Healthcare 3.0 witnessed an increase in the use and development of wearable technology in the form of smartwatches and trackers. Healthcare 4.0, the latest iteration, has taken steps towards actively enhancing medical procedures through the integration of networked devices. This application finds its greatest utility within the domains of telesurgery [2] and remote patient analysis. Latest computer technologies like Artificial Intelligence (AI), Machine Learning (ML), and the Medical Internet of Things (MIoT) can be used to facilitate medical procedures and consultations remotely.

The aforementioned technique of telesurgery has the potential to be utilised in various conventional medical procedures and disciplines, including endoscopy, laparoscopy, cardiology, kidney-related interventions, and dermatological treatments. Several high-risk, and dangerous procedures can also be automated or assisted with the help of robotic telesurgery. This sees many applications in the field of cardiology in procedures like mitral valve replacements, and coronary artery bypass surgeries with robotic tools making it less invasive than open-heart surgery. Kidney procedures like partial nephrectomy are also being performed with robotic assistance. Telesurgery is gaining traction in the domain of dermatology and associated treatments, mostly owing to its ability to enable distant consultations and diagnoses. A considerable proportion of dermatological operations can be effectively executed using telesurgery and robotic instruments as viable alternatives ensuring accuracy while also expediting the process of consultations and diagnoses.

Advancements in the field of skin-related applications are currently focused on the diagnosis of skin cancer. The determination of malignancy in skin cancer diagnosis involves the consideration of multiple parameters. Some factors in determining the presence of cancerous cells from an image of the skin tissue include melanocytic nevi, and basal cell carcinoma which develops on areas of the skin which are exposed to the sun. Actinic keratosis is a rough and scaly patch which can be seen on the skin due to a sun exposure for a long time, usually years. Dermatofibroma, another attribute used in the process, is an entity within the skin's dermis, which is usually benign but is more likely to metastasize. Vascular lesions, which we commonly call birthmarks, can fall under benign, locally aggressive, or malignant. Squamous cell carcinoma is an important factor in determination as it is a common type of skin cancer. Skin cancer is witnessing rising rates of occurrence globally. As per the World Health Organisation (WHO) [3], skin cancer is the most prevalent form of cancer on a global scale, accounting for more than 5 million annual diagnoses. In 2020, an estimated 57,000 deaths occurred among 325,000 projected melanoma cases, resulting in a mortality rate of approximately 17%, equating to 1 in 5 melanoma cases leading to death.

There has been a lot of research targeting the aforementioned issue of skin cancer detection using cell and lesion images. GoogleNet, a special kind of CNN was used to extract features from the images of Brain MRI in [4] by Sekhar *et al.* After extraction Support Vector Machine (SVM), Softmax and K Nearest Neighbor (KNN) were to classify these images. Shah *et al.* [5] provided a comprehensive study on skin cancer detection mechanism using Artificial Neural Network (ANN) and Convolution Neural Network (CNN). Tembhurne *et al.* [6] highlighted how an ensemble based mechanism of Deep Learning (DL) and ML can be used for this purpose. Hossen *et al.* [7] proposed an idea of using Federated ML technique for the enhancement in the IoMT sector in detecting skin cancer. Imran *et al.* in [8] showed how more than one individual deep learners like ResNet, VGG, CapsNet can be used simultaneously to achieve better and more accurate results in detection of skin cancer. Roy et al. in [9] underscored the use of robotics in the medical field. It mainly focuses on the use of robotics in surgery and healthcare.

Usually, AI is considered a 'black-box' due to its lack of explanation regarding the internal knowledge and implementation details. For the filed of healthcare, explanation is crucial as the internal workings of procedures must be known. Therefore, we propose X-*CaD* using eXplainable Artificial Intelligence (X-AI) in integration with Healthcare 4.0 for the detection of skin diseases. X-*CaD* employs MobileNet and Residual Neural Network (ResNet) with Integrated Gradient (IG) and Local Interpretable Model-agnostic Explanations (LIME) mechanisms. The objective of this approach is to present an X-AI mechanism that utilises images of skin tissue anomalies as its input received from remote patient side and provide alert towards telesurgoun and medical professional with proper interpretation.

A. Research Contribution

Following are the research contributions of the proposed approach:

- The proposed approach i.e., X-*CaD*, pioneers telesurgery applications in skin-related procedures and cancer detection, transforming remote patient surgery by leveraging advanced technologies and enabling efficient and precise interventions beyond traditional surgical boundaries..
- By leveraging advanced CNN architectures, ResNet and MobileNet, X-*CaD* introduces a robust mechanism for binary classification, ensuring accurate identification of skin cancer in dermoscopic images for telesurgery applications.
- Revealing the intricate decision-making processes of AI, X-*CaD* utilizes LIME and IG techniques to enhance interpretability in CNN models. This contribution ensures transparent and clinically insightful decision-making, crucial for the effectiveness of telesurgery in skin cancer detection.

B. Organization of the Paper

The rest of the paper is organized as follows. Section II presents the system model and problem formulation. Section III elaborates the proposed approach in detail. Section IV highlights the performance evaluation of the proposed approach. Finally, the paper is concluded with future work in Section V.

II. System model and problem formulation

This section delves into the system model and problem formulation of the proposed approach.

A. System Model

In a remote patient ($\mathcal{P}$) telesurgery environment, the proposed system is designed to facilititae the detection of various skin conditions, including Melanoma ($\mathcal{S}_1$), Melanocytic nevus ($\mathcal{S}_2$), Basal cell carcinoma ($\mathcal{S}_3$), Dermatofibroma ($\mathcal{S}_4$), Vascular lesion ($\mathcal{S}_5$), and Squamous cell carcinoma ($\mathcal{S}_6$), using a CNN architecture. The process initiates with the acquisition of dermoscopic/macroscopic images (I) from the patient's location, facilitated by a dermatoscope (ξ) equipped with high-resolution imaging sensors. Macroscopic images (I) refer to high-resolution photographs of a lesion, which effectively depict its comprehensive characteristics such as dimensions, configuration, pigmentation, and surface topography. In order to maintain a constant level of image quality, it is imperative that the dermatoscope be equipped with a standardised illumination system. Subsequently, the acquired images undergo compression and encryption procedures employing robust protocols (τ), such as Message Queuing Telemetry Transport (MQTT) and Real-Time Transport Protocol (RTP), in order to guarantee the preservation of data integrity and confidentiality during the transmission process to the telesurgery centre.

The telesurgery center's edge computing device preprocesses transmitted images, incorporating operations like enhancement, noise reduction, and segmentation to prepare ($X_{\text{pre-processeds}}$) for binary classification by a CNN-based model (Λ_{CNN}). This architecture extracts discriminative features, enabling accurate binary categorization of skin lesions as cancerous (C_1) or benign (C_0). The output (Θ) represents the probability of skin cancer (θ_{cancer}), compared to a predefined threshold ($T_{threshold}$) for cancer detection. Upon a cancer determination, the X-AI module engages LIME (Π_1) and IG (Π_2) to offer localized explanations, pinpointing regions impacting the cancer prediction. These explanations provide insights into the regions of interest within the images that influenced the cancer diagnosis. The combination of CNN classification results (Θ) and X-AI based explanations (Π, here $\{\Pi_1, \Pi_2\} \in \Pi$) serves as the final diagnostic output (Ω), which is transmitted to the telesurgeon and medical authorities for clinical evaluation. By utilising AI-driven diagnostic tools and explanatory systems, the telesurgeon is able to make informed decisions regarding the optimal approach for performing dermatological surgery on a patient located remotely. This process ensures transparency and facilitates informed decisions in remote dermatological surgery.

B. Problem Formulation

This section provides insight into the problem formulation process for suggested X-*CaD* approach. The acquisition of

dermoscopic/macroscopic images (I) from patients ($\mathcal{P}$) is a pivotal phase driven by the dermatoscope (ξ). This process is encapsulated by the function shown in Eq. 1.

$$I = \xi(\mathcal{P}) + \eta(\xi, \mathcal{S}_i) \tag{1}$$

here, I represents the collection of acquired images, while ξ encompasses the complexities of the dermatoscopic image capturing process, taking into account the variations within the patient set $\mathcal{P}$ and $\eta(\xi, \mathcal{S}_i)$ models the stochastic aspect related to skin condition representation. The secure transmission of images (I) involves encryption and compression mechanisms as shown in Eq. 2 using standard MQTT and RTP protocols framework (τ) to ensure the integrity and confidentiality of transmitted data.

$$I_{\text{transmitted}} = \tau(I) \tag{2}$$

The pre-processing phase leading to the input data for the CNN model, denoted as $X_{\text{pre-processed}}$, can be expressed as follows:

$$X_{\text{pre-processed}} = \phi(I_{\text{transmitted}}) \tag{3}$$

here, the function ϕ encompasses a collection of techniques including image enhancement, noise reduction, and segmentation, which serve as the foundation for subsequent advanced analyses.

The binary classification output (Θ) of the CNN model (Λ_{CNN}), signifies the probability of skin cancer presence and utilization of $X_{\text{pre-processed}}$ as seen in Eq. 4. By means of this intricate conversion, discernible characteristics are extracted from images that have been preprocessed, resulting in a more sophisticated comprehension of skin lesions. Eq. 5 represents the binarycross-entropy loss function, which quantifies the discrepancy between the probabilities predicted and the labels of the ground truth.

$$\Theta = \Lambda_{CNN}(X_{\text{pre-processed}}) \tag{4}$$

$$L(\Theta, C_1, C_0) = -(C_1 \cdot \log(\theta_{cancer}) + C_0 \cdot \log(1 - \theta_{cancer})) \tag{5}$$

The generation of locally interpretable explanations by the X-AI module is an essential component, as denoted by Eq. 6. In this context, Π reveals detailed insights into the CNN's decision-making process, thereby adding an interpretable and transparent layer to the complex opaqueness of CNN architecture.

$$\Pi = \text{X-AI}(\Theta) \tag{6}$$

A weighted sum of the CNN (Λ) classification results and LIME and IG-based explanations (Π) constitutes the final diagnostic output Ω towards telesurgeons, medical authorities, and dermatology diagnostic practitioners. By adjusting the weights of the two terms, one can determine which factor is more crucial in the decision-making process. For instance, in the case where the telesurgeon prioritises accountability and transparency, they might assign greater significance to the explanations derived from LIME.

III. THE PROPOSED SCHEME

Fig. 1 depicts proposed approach. X-*CaD* comprises four main layers: a data acquisition and transmission layer, an DL layer for processing, an X-AI layer, and a telesurgery alert layer.
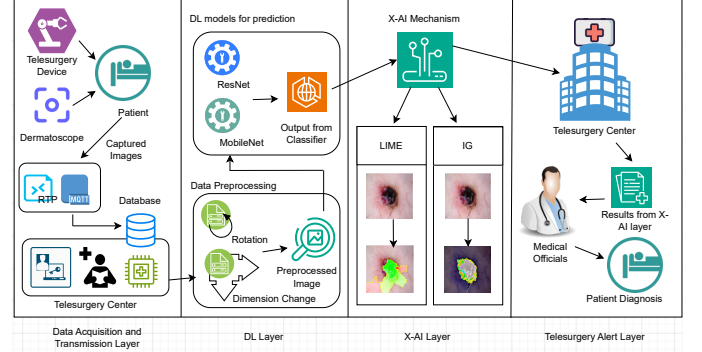

Fig. 1: proposed X-*CaD* approach.

A. Data Acquisition and Transmission Layer

The data consists of patient information ($\mathcal{P}_i$, where, $\mathcal{P}_i \in \mathcal{P}$) obtained using ξ, which is a medical device used for the examination of skin lesions. As seen in Eq. 7, dermatoscope process ($\xi(\mathcal{P}_i)$) is augmented by a Laplacian operator ∇. Where, ∇^2 captures additional spatial variations that are introduced during the process of image acquisition. By reflecting the second-order spatial derivatives, this operator offers a more sophisticated depiction of the influence that ξ has on the process of acquiring data. The utilisation of the nested integral over dS_{latent} remains crucial in the modelling of stochastic representations of skin conditions. In this way, comprehensive equation incorporates both the individualised patient variations and the complex process of dermatoscopic capture in a more sophisticated and refined manner.

$$I = \int_{\mathcal{P}} \left[\xi(\mathcal{P}_i) \cdot \left(1 + \int_{S_{\text{latent}}} \eta(\xi, \mathcal{S}_i) \, dS_{\text{latent}} \right) \right] \cdot \left(1 + \nabla \cdot \nabla^2 \xi(\mathcal{P}_i) \right) d\mathcal{P}_i \tag{7}$$

The data transfer to the telesurgery center employs secure MQTT and RTP protocols, ensuring robust transmission. Advanced cryptographic methods, including wavelength transformation ($\mathcal{W}$) for in-depth frequency analysis, alongside specific key functions $\mathcal{K}$encrypt and $\mathcal{K}$compress, address telesurgery intricacies. Where, the encryption process (ϵ) is utilised as a reliable method to maintain the integrity of image, while the compression procedure (κ) plays a crucial role in optimising the utilisation of bandwidth, which is a significant factor to consider in real-time telesurgery applications as seen in Eq. 8. This process aligns with remote patient operations, utilizing MQTT for lightweight messaging and RTP for real-time traffic handling over UDP. The amalgamation of cryptographic techniques and secure protocols ensures seamless integration

of dermoscopic data into telesurgery, enabling real-time and reliable remote patient procedures.

$$I_{\text{transmitted}} = \epsilon\left(\kappa\left(\mathcal{W}(I, \mathcal{K}_{\text{encrypt}}), \mathcal{K}_{\text{compress}}\right)\right) + \delta(\eta_{\text{MQTT-RTP}})$$
(8)

here, δ represents the incorporation of secure transmission protocols and $\eta_{\text{MQTT-RTP}}$ encompasses the distinct factors associated with the protocols MQTT and RTP.

B. DL Layer

The DL layer in X-*CaD* acquires a critical role in the detection of skin cancer for telesurgery environment, utilising advanced CNN architectures such as MobileNet ($\Lambda_{\text{MobileNet}}$) and ResNet ($\Lambda_{\text{ResNet}}$). Dermoscopic images from a balanced dataset [10]–[13] of 8,251 images, with 4,523 labeled as 1 (malignant conditions) and 3,728 as 0 (non-cancerous), are used for training. Label 1 denotes imgaies that exhibit characteristics associated with malignant conditions, specifically basal cell carcinoma, melanoma, actinic keratosis, and vascular lesions. Label 0 denotes images depicting dermatofibroma, benign keratosis, solar lentigo, and seborrheic keratosis, which are all non-cancerous conditions. The data is split into train, test, and validation sets with a distribution of 90-10 for train-test and 80-20 for train-validation.

The images undergo pre-processing, involving body hair removal and masking for lesion isolation, scaling, zooming, shearing etc. and preparing $X_{\text{pre-processed}}$ for Λ using the function ϕ. The pre-processing function ϕ represents a sequence of sophisticated differentiable transformations that include adaptive activation functions and parameters that can be learned as seen in Eq. 9. These techniques guarantee that the models are capable of accurately identifying pertinent features for precise detection of skin cancer in dermoscopic images, thereby enhancing the overall effectiveness of X-*CaD*.

$$\phi = \sigma_{\text{adaptive}}(\mathcal{H}_{\text{rot}} \circ \mathcal{H}_{\text{shift}} \circ \mathcal{H}_{\text{scale}} \circ \mathcal{H}_{\text{shear}} \circ \mathcal{H}_{\text{zoom}} \circ \mathcal{H}_{\text{flip}})$$ (9)

here, σ_{adaptive} represents an adaptive activation function, and $\mathcal{H}_{\text{rot}}, \mathcal{H}_{\text{shift}}, \mathcal{H}_{\text{scale}}, \mathcal{H}_{\text{shear}}, \mathcal{H}_{\text{zoom}}, \mathcal{H}_{\text{flip}}$ are advanced differentiable transformations incorporating learnable parameters.

X-*CaD* utilizes CNN architecture to identify the skin cancer in telesurgery environment. $X_{\text{pre-processed}}$ will further be served as input for Λ. In here, $\Lambda_{\text{MobileNet}}$ and Λ_{ResNet} architectures are utilized as the convolutional base. These architectures serve as the foundation for feature extraction, which is critical for identifying subtle patterns that indicate skin anomalies. The MobileNet architecture, recognized for its computational efficiency, employs depthwise separable convolutions as seen in Eq. 10. It features sequential depthwise separable convolutional and pointwise convolutional layers, each followed by batch normalization, ReLU activation, and a dense layer with 32 neurons. In parallel, the ResNet architecture, known for its residual learning framework as shown in Eq. 11, integrates residual blocks with batch normalization, ReLU activation, and convolutional layers. This approach mitigates the vanishing gradient problem, enhancing training effectiveness. Both architectures conclude with a sigmoid-activated neuron for binary classification (C_0 and C_1). Training utilizes the Adam optimizer with a learning rate initially set to 0.001,

which is adjustable based on validation accuracy for improved convergence.

$$\Lambda_{\text{MobileNet}}(X_{\text{pre-processed}}; \Theta_{\text{MobileNet}}) =$$
$$\text{DSConv}(\text{PWConv}(\text{BN}(\text{ReLU}(\text{DSConv}(\dots)))))$$
(10)

$$\Lambda_{\text{ResNet}}(X_{\text{pre-processed}}; \Theta_{\text{ResNet}}) = X_{\text{pre-processed}} +$$
$$\text{RSDBlock}(\dots + \text{RSDBlock}(\text{BN}(\text{ReLU}(\text{Conv}(\dots)))))$$
(11)

$$\Theta = \text{Dense}(\text{Dropout}(\text{GAP}(\Theta_{\text{MobileNet}} + \Theta_{\text{ResNet}})))$$ (12)

C. X-AI Layer

The CNN model, denoted as Λ, performs binary classification (Θ) to determine the presence of cancer in the input data. However, the conventional 'black-box' nature of AI becomes undesirable, particularly when dealing with cancer cases. In the medical field, the need for explanation and reasoning behind diagnoses is crucial, as healthcare providers are accountable to their patients. Therefore, X-AI plays a pivotal role in X-*CaD*, providing essential explanations and insights into the model's workings and mechanisms to ensure transparency and trust in the diagnostic process. In our approach, we leverage LIME [14] as Π_1 and IG [15] as Π_2, powerful tools in healthcare for constructing localized, simplified models around specific predictions. Π_1 as in Eq. 13 and in Eq.14enhances information from an already trained CNN model, with the pre-trained model and dataset fed into Π_1 with specific adjustments. Π_1 learns the decision-making process of Λ_{CNN}, yielding component-specific explanations that visually interpret the output Θ from the preceding layer, Eq.14 shows the LIME interpretation process. The process involves transforming the input image and leveraging LIME's explainer to generate locally faithful explanations for model predictions.

$$\theta_{Visualised1} = \Pi_1(\Lambda_{CNN}, \pi, X_{\text{pre-processed}})$$ (13)

$$\Pi_{\text{LIME}}(f, \pi, x) = \underset{g \in G}{\text{argmin}}\left(\mathcal{L}(f, g, \pi, x) + \Pi(g)\right)$$
$$\text{where} \quad \mathcal{L}(f, g, \pi, x) = \sum_{z \in Z} \pi(z)\left(f(x) - g(x, z)\right)^2$$
$$\text{and} \quad \Pi(g) = \Pi_{\text{comp}}(g) + \Pi_{\text{simp}}(g)$$
$$\text{with} \quad \Pi_{\text{comp}}(g) = \lambda \cdot \text{complexity}(g)$$
$$\text{and} \quad \Pi_{\text{simp}}(g) = (1 - \lambda) \cdot \text{simplicity}(g)$$
(14)

here, Π_{LIME} represents LIME's explanation output for model f, instance x, and perturbation distribution π. Optimization over interpretable models G minimizes the dissimilarity between the original model's prediction and g on perturbed instances, regulated by complexity $\Pi_{\text{comp}}(g)$ and simplicity $\Pi_{\text{simp}}(g)$, balanced by hyperparameter λ.

X-*CaD* also uses IG as Π_2 which is a method that maps the output of the model to its input. This process is done by considering the data of the class 1, i.e., the malignant class samples and calculating the gradient(g) with respect to this data through a series of linear interpolations. The resultant values are integrated over this data as seen in Eq. 15.

$$\Pi_{\text{IG}}(f, \pi, x) = \int_g \left(Xmal_{\text{pre-processed}} \cdot \nabla_{g_i}\right) \circ dg_i$$ (15)

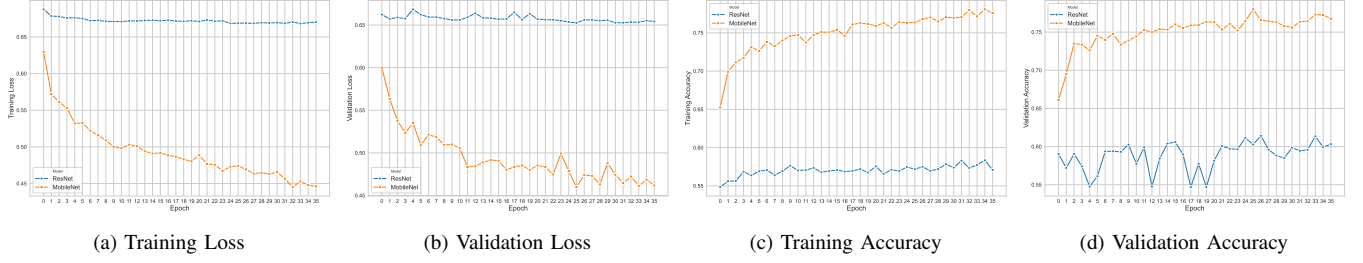| (a) Training Loss | (b) Validation Loss | (c) Training Accuracy | (d) Validation Accuracy |

Fig. 2: (a) Loss curve for different models during the training, (b) Loss curve for different models during the validation, (c) Accuracy curve for different models during the training, (d) Accuracy curve for different models during the validation

here, $Xmal_{\text{pre-processed}}$ represents the images of the malignant class. Finally after loading the pretrained model to IG and the input image we get the output θ in the form of heat map which underscores and explain which the images is classified as malignant by the model Λ_{CNN}.

$$\theta_{Visualised2} = \Pi_2(\Lambda_{CNN}, \pi, X_{\text{pre-processed}}) \quad (16)$$

The layer Π is thus a combination of Π_1 and Π_2, i.e., $\Pi = \Pi_1 + \Pi_2$.

D. Telesurgery Alert Layer

The telesurgery center receives the data as Ω which is the weighted sum of two components, the output from the model Λ_{CNN} and the output from the X-AI layer Π.

$$\Omega = w_1 \Lambda_{CNN}(X_{\text{pre-processed}}) + w_2 \Pi(X_{\text{pre-processed}}) \quad (17)$$

In the given Eq. 17 weights w_1 and w_2 are adjusted by the officials at the telesurgery center as per their requirement of information from each of the components. $\delta = \frac{w_1}{w_2}$ is the ratio of both weights, if δ is more, Ω is inclined towards the output Λ_{CNN}. Inversely, Ω is inclined towards Π. This information provides valuable acumen to the higher medical authorities at the telesurgery center based on which they take the important decisions. The confidentiality and integrity of the critical data is maintained using various protocols in a secured environment taking into account the latest standard of laws pertaining to privacy of an individual. Thus X-AI in the medical sector increases the transparency and clarity of the results obtained unlike traditional 'black-box' techniques.

IV. PERFORMANCE EVALUATION

This section presents the performance evaluation of X-*CaD*. This section is further divided into two major parts, one DL-based CNN architecture model performance evaluation on training and validation datasets. The second is the adaptation and interpretation of X-AI approaches for MobileNet, which gave greater convergence and validation accuracy.

A. CNN based Results

The evaluation of X-*CaD* ensures uniformity in computation resources by conducting training on the NVIDIA GPU P100, renowned for its parallel processing capabilities, featuring 3,584 CUDA cores and 16 GB HBM2 memory. Both ResNet50V2 and MobileNetV2 undergo 35 epochs of training
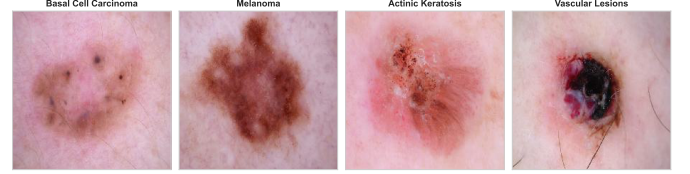

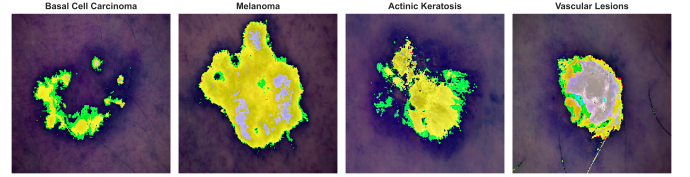Fig. 3: Original class 1 images.

Fig. 4: Integrated gradient output by $\Lambda_{\text{MobileNet}}$ model on class 1 images

with Adam optimizer and binary cross-entropy loss function for binary classification. To enhance stability, we incorporate a dynamic learning rate adjustment and EarlyStopping to monitor validation accuracy as mentioned in Section III. The adoption of this standardised approach ensures that comparison analysis is unbiased and reliable, leading to consistent outcomes when evaluating the performance of ResNet and MobileNet.

The results obtained with ResNet and MobileNet under training and validation conditions can be observed in Fig. 2. Fig. 2a shows how the training loss values for MobileNet are much lower as compared to the ResNet. By the 35th epoch, MobileNet has a loss of 0.20 lesser than ResNet. A similar trend can be observed in the validation loss in Fig. 2b, where by the 35th epoch, the loss difference is again 0.20 in the favour of MobileNet. The accuracy values for training can be observed in Fig. 2c with MobileNet having an initial accuracy of 0.65, eventually reaching over 0.75 by the 35th epoch. ResNet shows an accuracy of 0.55 initially, and reaches just over 0.55 by the 35th epoch. For the validation accuracy is shown in Fig. 2d wherein MobileNet displays an accuracy of 0.65 to an eventual 0.75 whereas ResNet exhibits an accuracy of 0.60. These observations show how MobileNet has a better accuracy than ResNet, accompanied by a lower loss in both the training and validation conditions. The validation loss serves as a crucial metric in assessing the performance of the model. A lower loss value indicates that the

network has effectively converged, stabilizing its parameters to yield accurate predictions. In this particular situation, the process of convergence is observed when the network reaches a significant loss value of 0.45. This value indicates the stability and accuracy of the network in making predictions based on the given data. The achievement of high accuracy at the convergence point serves as evidence of the network's successful deployment in producing effective outcomes.
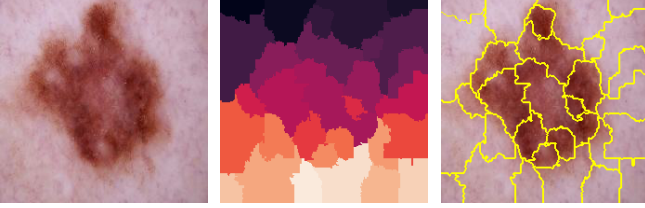

Fig. 5: Class 1 images: original image, LIME segment, LIME superpixel segment for Melanoma
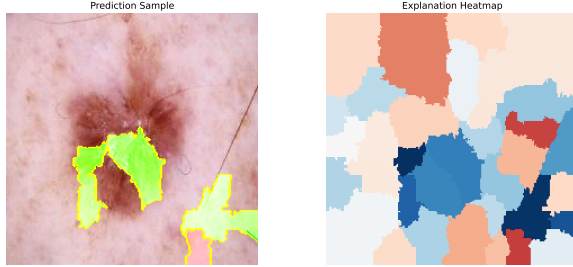

Fig. 6: LIME output for class 1 along with it's heat map, 6 number of features and 1000 number of samples for Melanoma

B. X-AI Results

Unlike the traditional 'black-box', X-*CaD* uses X-AI to represent output from the DL layer in a way that provides valuable information, on why the data was classified as malignant, to the medical authorities which help them take important decisions in the medical treatment of the patient. X-*CaD* uses LIME and IG to give the required X-AI result, additionally $\Lambda_{MobileNet}$ is used to gain better results in this direction. To demonstrate the results four images from the dataset which are labelled as cancerous are considered as shown in Fig. 3. These images are the lesion images of the categories Basal Cell Carcinoma, Melanoma, Actinic Keratosis, Vascular Lesions respectively. Fig. 4 shows the result when these images when fed to Π_2 IG X-AI in the form of heat map. In the heatmap, warmer colors denote higher attribute values, signifying the regions influencing the cancerous classification of the image.

For the results of LIME Melanoma lesion and vascular lesion images were taken as input. The melanoma input image, corresponding LIME segments and LIME superpixel segment are shown in Fig. 5. LIME segments represent the segmentation of the image which is an input for the Π_1. Further the pixels are grouped using superpixel segmentation technique and we get defined boundary for each segment and finally heat map is created as the output which represents the extent
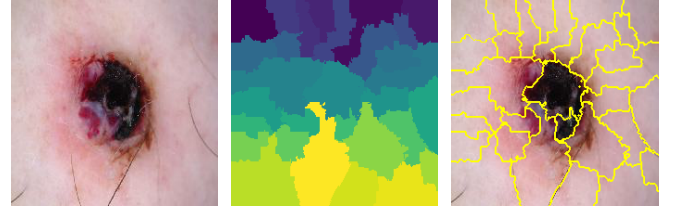

Fig. 7: Class 1 images: original image, LIME segment, LIME superpixel segment for Vascular Lesions
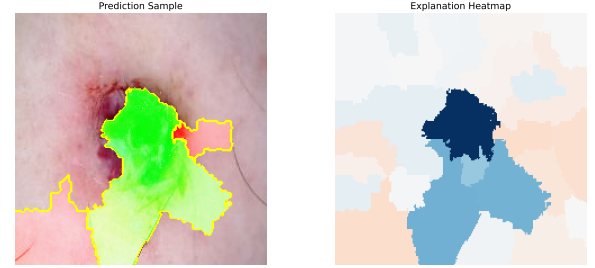

Fig. 8: LIME output for class 1 along with it's heat map, 6 number of features and 1000 number of samples for Vascular Lesions

to which each segment was responsible for the classification of image as cancerous. The output in the form of heat map is shown in Fig. 6 which includes the prediction sample along with the it's explanatory heat map. In this heat map the colder color represent the segment of image due to which the image is classified as cancerous by the $\Lambda_{MobileNet}$. Another image of cancerous Vascular lesion from the dataset was fed to Π_1. The input image, LIME segment and corresponding superpixel segmentation are shown in Fig. 7 and the output in the form of heat map is displayed in Fig. 8.

V. CONCLUSION AND FUTURE SCOPE

In conclusion, our suggested approach utilises sophisticated CNN architectures, namely ResNet and MobileNet, in conjunction with X-AI techniques such as LIME and IG, to augment the comprehensibility of skin cancer diagnosis in telesurgery environment. By unraveling the black-box nature of AI models, we contribute to transparent decision-making processes crucial for effective clinical applications. Future work involves exploring the integration of blockchain technology in telehealth applications for heightened security and privacy. Additionally, further refinements in CNN and X-AI models are essential for continuous improvement in the accuracy and reliability of skin cancer diagnoses in telesurgery environments.

REFERENCES

[1] K. Raparla, N. Pandey, and S. Modh, "Indigenous and disruptive remote patient monitoring devices - a case study on ai in healthcare," *SDMIMD Journal of Management*, vol. 14, pp. 27–34, 09 2023.

[2] R. Gupta, S. Tanwar, S. Tyagi, and N. Kumar, "Tactile-internet-based telesurgery system for healthcare 4.0: An architecture, research challenges, and future directions," *IEEE Network*, vol. 33, no. 6, pp. 22–29, 2019.

[3] W. H. Organization, "Radiation: Ultraviolet (uv) radiation and skin cancer," 2023.

[4] A. Sekhar, S. Biswas, R. Hazra, A. K. Sunaniya, A. Mukherjee, and L. Yang, "Brain tumor classification using fine-tuned googlenet features and machine learning algorithms: Iomt enabled cad system," *IEEE Journal of Biomedical and Health Informatics*, vol. 26, no. 3, pp. 983–991, 2022.

[5] A. Shah, M. Shah, A. Pandya, R. Sushra, R. Sushra, M. Mehta, K. Patel, and K. Patel, "A comprehensive study on skin cancer detection using artificial neural network (ann) and convolutional neural network (cnn)," *Clinical eHealth*, vol. 6, pp. 76–84, 2023.

[6] J. V. Tembhurne, N. Hebbar, H. Y. Patil, and T. Diwan, "Skin cancer detection using ensemble of machine learning and deep learning techniques," *Multimedia Tools and Applications*, vol. 82, pp. 27501–27524, Jul 2023.

[7] M. N. Hossen, V. Panneerselvam, D. Koundal, K. Ahmed, F. M. Bui, and S. M. Ibrahim, "Federated machine learning for detection of skin diseases and enhancement of internet of medical things (iomt) security," *IEEE Journal of Biomedical and Health Informatics*, vol. 27, no. 2, pp. 835–841, 2023.

[8] A. Imran, A. Nasir, M. Bilal, G. Sun, A. Alzahrani, and A. Almuhaimeed, "Skin cancer detection using combined decision of deep learners," *IEEE Access*, vol. 10, pp. 118198–118212, 2022.

[9] A. Halder Roy, S. Ghosh, and B. Gupta, "Robotics in medical domain: The future of surgery, healthcare and imaging," *Wireless Personal Communications*, vol. 132, pp. 2885–2903, Oct 2023.

[10] https://www.kaggle.com/datasets/mehdiuniv/balanced datasets/data

[11] P. Tschandl, C. Rosendahl, and H. Kittler, "The ham10000 dataset: A large collection of multi-source dermatoscopic images of common pigmented skin lesions," *Scientific Data*, vol. 5, 08 2018.

[12] N. C. F. Codella, D. Gutman, M. E. Celebi, B. Helba, M. A. Marchetti, S. W. Dusza, A. Kalloo, K. Liopyris, N. Mishra, H. Kittler, and A. Halpern, "Skin lesion analysis toward melanoma detection: A challenge at the 2017 international symposium on biomedical imaging (isbi), hosted by the international skin imaging collaboration (isic)," in *2018 IEEE 15th International Symposium on Biomedical Imaging (ISBI 2018)*, pp. 168–172, 2018.

[13] M. Combalia, N. C. F. Codella, V. M. Rotemberg, B. Helba, V. Vilaplana, O. Reiter, A. C. Halpern, S. Puig, and J. Malvehy, "Bcn20000: Dermoscopic lesions in the wild," *ArXiv*, vol. abs/1908.02288, 2019.

[14] M. T. Ribeiro, S. Singh, and C. Guestrin, "Why should i trust you? explaining the predictions of any classifier," in *Proceedings of the 22nd ACM SIGKDD International Conference on Knowledge Discovery and Data Mining*, pp. 1135–1144, ACM, 2016.

[15] Y. Zhuo and Z. Ge, "IG2: Integrated Gradient on Iterative Gradient Path for eXplainable AI," 9 2023.